HAL open science

Synthesis and Study of the Application of Iron, Nitrogen-Doped High-Surface-Area Carbon for Li–S Batteries

Sajad Rahimi, Laureline Lecarme, Nathalie Job, Fannie Alloin

To cite this version:

Sajad Rahimi, Laureline Lecarme, Nathalie Job, Fannie Alloin. Synthesis and Study of the Application of Iron, Nitrogen-Doped High-Surface-Area Carbon for Li–S Batteries. ACS Applied Materials & Interfaces, 2025, 17 (26), pp.38031-38040. ⟨10.1021/acsami.5c05993⟩. ⟨hal-05160018⟩

HAL Id: hal-05160018

https://hal.science/hal-05160018v1

Submitted on 12 Jul 2025

HAL is a multi-disciplinary open access archive for the deposit and dissemination of scientific research documents, whether they are published or not. The documents may come from teaching and research institutions in France or abroad, or from public or private research centers.

L'archive ouverte pluridisciplinaire **HAL**, est destinée au dépôt et à la diffusion de documents scientifiques de niveau recherche, publiés ou non, émanant des établissements d'enseignement et de recherche français ou étrangers, des laboratoires publics ou privés.

Distributed under a Creative Commons CC BY 4.0 - Attribution - International License

Synthesis and study of the application of Iron, Nitrogen-doped high surface area carbon for Li-S batteries

Sajad Rahimi[†], Laureline Lecarme[†], Nathalie Job[§], Fannie Alloin[†,ŧ *]

[†] Univ. Grenoble Alpes, Univ. Savoie Mont Blanc, CNRS, Grenoble INP, LEPMI, 38000 Grenoble, France
[§] Department of Chemical Engineering - NCE (Nanomaterials, Catalysis, Electrochemistry), University of Liège, 4000 Liège, Belgium
[ŧ] Réseau sur le Stockage Electrochimique de l'Energie (RS2E), CNRS, FR3459, 80 039 Amiens Cedex, France

Corresponding author e mail: Fannie.alloin@grenoble-inp.fr

Keywords: Lithium Sulfur Battery, lean electrolyte, high sulfur content, nitrogen-doped carbon, iron particle.

Abstract

Despite their promising theoretical performance, lithium-sulfur (Li-S) batteries are often limited by low efficiency, primarily due to the solubility of lithium polysulfides and the low conductivity of sulfur electrodes. Enhancing the incorporation of sulfur into porous carbon with improved polarity could significantly boost Li-S battery performance. In this study, we doped carbon xerogels with nitrogen atoms and decorated them with iron-based nanostructures using a straightforward and scalable method. The decomposition of nitrogen-containing additives at varying temperatures—specifically 750°C (FeNC-750) and 950°C (FeNC-950) resulted in alterations to the porosity of the xerogel compared to the pristine structure. After impregnating these structures with sulfur to develop the sulfur electrode, we assessed the electrochemical performance of FeNC-750@S and FeNC-950@S, varying the sulfur content and the electrolyte-to-sulfur (E/S) ratio. Our results indicated that the electrochemical performance of the sulfur electrode with high sulfur content was significantly influenced by both the E/S ratio and the porosity of the host materials. Notably, the sulfur electrode with over 80% sulfur content, designated FeNC-950@S_{80}, achieved a discharge capacity of 600 mAh g^{-1} with an E/S ratio of 7.5 mL g^{-1} and an electrode loading of 3.5 g cm^{-2}, demonstrating excellent capacity retention of 96% over 100 cycles at a rate of 0.1 C.

Introduction

Despite the overwhelming advantages of lithium sulfur (Li-S) batteries, this system faces several challenges, which must be overcome for commercial application. These issues mostly originate from the inherent characteristics of the materials involved, such as low electronic conductivity of sulfur and Li_2S, large volume changes of the active material during charge and discharge processes, and more importantly the presence of lithium polysulfides (LiPSs), *e.g.* intermediate active species, which are soluble in the electrolyte. These challenges limit cyclic stability, cause low coulombic efficiency, positive electrode collapsing, low voltage efficiency, and low battery lifetime[1-5].

Recently, by employing new sulfur host materials[6-9], or by developing new interlayers[10, 11] and electrolytes[12, 13], important steps have been taken toward the commercialization of Li-S batteries in terms of improving specific capacity and cycle life. Over the past decade, researchers have proposed various advanced carbon materials as sulfur host to enhance the performance of positive electrodes and mitigate the polysulfide shuttle effect. Studies have investigated a range of sulfur host materials, including carbon black[14-17], carbon nanotubes[18-20], graphene[21-23], heteroatom-doped carbonaceous materials[24-29], or metal-based structures[30-33]. Porous carbons are particularly attractive for high-performance sulfur electrodes due to their excellent mechanical stability and high void fraction.

On one hand, carbon micropores effectively confine short-chain LiPSs, while on the other hand, carbon mesopores serve as channels that facilitate mass transport[28]. Despite these advantages, the low polarity of carbon materials leads to suboptimal electrochemical performance in Li-S batteries. To overcome this limitation, doping the carbon backbone with polar atoms or impregnating it with polar compounds has been identified as an effective strategy to enhance carbon polarity[34-36]. In addition to doping carbon with heteroatoms like nitrogen to enhance surface polarity, impregnating carbon materials with iron-based compounds can also effectively address this non-polarity challenge[37, 38]. Iron atoms can form various phases depending on the synthesis conditions, including single atoms[39], carbides[40], nitrides[41, 42], oxides[43], sulfides[19, 44], and others, all of which can effectively anchor LiPSs to the positive electrode, in the sulfur host materials including iron-based phases.

A well-designed sulfur host material must possess several essential characteristics: (i) excellent electrical conductivity to ensure efficient electron transport and address the low electrical conductivities of sulfur and lithium sulfide (Li_2S), (ii) a large pore volume with a stable structure to accommodate volume expansion due to the lower density of Li_2S compared to S_8, which helps prevent electrode pulverization during cycling, (iii) a high surface area to facilitate the conversion reactions of sulfur—especially at high sulfur content—and the deposition of Li_2S, (iv) sufficient polarity to interact with LiPSs, thereby mitigating the shuttle effect and loss of active materials, [45] (v) enhanced conversion kinetics of LiPSs redox reactions through the incorporation of electrocatalytic species[46], and (vi) their development for commercial applications must be both feasible and cost-effective.

Herein, we designed sulfur host materials by considering the above-mentioned characteristics. First, a carbon xerogel which can be described as an assembly of microporous nodules delimiting meso and microporous voids was used as the carbon support to physically confine sulfur and LiPSs and ensure the required mechanical properties of the electrode. In the next step, the carbon xerogel was doped with nitrogen and iron-based compounds. Melamine and Fe^{II} were utilized for doping and decorating the porous carbon with nitrogen atoms and iron-based compounds, respectively, *via* a simple pyrolysis process. The pyrolysis was performed at various temperatures to obtain different N-doped carbon host morphologies incorporating iron-based compounds. The catalytic behavior toward the LiPSs redox reactions was evaluated using cyclic voltammetry. The two host structures were then impregnated with S to synthesize FeCN-950@S and FeCN-750@S with different sulfur contents (60 wt. % and 80 wt. %). Finally, their electrochemical performance in terms of specific capacity and capacity retention in different electrolyte-to-sulfur ratio (E/S) conditions was evaluated and compared to those of the carbon xerogel host structure.

Experimental Section

Preparation of porous carbon xerogel. The synthesis of the porous carbon xerogel used as host was described in a previous report[47]. Briefly, the carbon xerogel with a mesoporous pore size of ~20 nm, determined by mercury porosimetry, was synthesized by the polycondensation of resorcinol (R) and formaldehyde (F) in an aqueous medium with specific pH using microwave. After polymerization, and evaporating the extra water, the dry material was collected and pulverized, then transferred to a tube furnace, and carbonized at 750°C under N_2 gas to obtain a porous carbon xerogel.

Melamine (Acros – chemical 99%) as the nitrogen precursor was mixed with the porous carbon in the mass ratio of 25 wt%. The mixture was dispersed in 50 mL of solvent mixture (v/v = 1/4) of deionized water and ethanol (VWR, 96%). The suspension was sonicated for 1 h then 1.5 wt% of $Fe(ac)_2$ (Acros – chemical 95%) *vs.* porous carbon and 4 mL ammonia solution (Fisher) were added and stirred for 3 h at 80 ℃ to evaporate the solvent. The powder was collected and transferred to a quartz tube furnace operating under N_2 gas for 1 h. The nature of the Fe particles environment was modified by varying the pyrolysis temperature (from 650 ℃ to 1000 ℃). After cooling down to room temperature the samples at 750 ℃ and 950 ℃ were selected to represent the N-doped carbon including Fe particles at 750℃ (FeCN-750), and at 950℃ (FeCN-950), and were used as the sulfur host materials.

Fe/CN@S, Fe_3C/CN@S preparation. The synthesized carbon host materials and the pristine carbon, for comparison purpose, were mixed with sulfur (Alfa Assar A7558) in the weight ratio of 2:3 and heated up to 160 ℃ under N_2 gas for 2 h to achieve sulfur impregnation. The active materials were labeled as FeCN-950@S_{60}, FeCN-750@S_{60} and C@S_{60}. To obtain the FeCN-950/CN@S_{80}, FeCN-750@S_{80} the weight ratio of 1:4 (host material/sulfur) was used with the same impregnation process.

Evaluation of the kinetics of the conversion process. In order to examine the effect of the synthesized materials on the kinetics of the LiPSs conversion reaction, the FeCN-750 and FeCN-950 compounds were mixed with polyvinylidene fluoride, (PVDF, Solvay Solef 6020/1001) in the ratio of 9:1, respectively. A viscous ink was made by adding several drops of N-methyl-2-pyrrolidone (NMP, Thermo Fisher Scientific, AcroSeal packaging) and stirring. Then, the obtained homogeneous ink was casted onto the surface of a platinum electrode (2 mm diameter). A three-electrode system, including Li metal as reference and counter electrode, and the carbon host structure as the working electrode, was used to characterize the FeCN-750, and FeCN-950 catalytic properties by cyclic voltammetry (CV). The electrolyte was 10 mM of Li_2S_6 in dioxolane (DOL, anhydrous, 99.8%, Aldrich)/dimethoxyethane (DME, Alfa Aesar) (1:1 in vol) + 1 M LiTFSI. CV was performed at different scan rates between 2.0 and 2.8 V *vs.* Li^+/Li. By measuring the ΔE_p at different scan rates, the kinetics constant (k^0) values of the Li_2S_6/Li_2S_4 reaction were calculated for the two host materials by using the Nicholson's method[48].

Materials characterizations. The morphology of the materials was characterized by scanning electron microscopy (SEM KARL ZEISS Ultra 55) with an electron energy of 5 keV. Conventional transmission electron microscopy (TEM) images were obtained by using a JEOL 2010 TEM microscope operated at 200 kV with a resolution of 0.19 nm. The amounts of iron were obtained by using a PinAAcle 900 Series of AA spectometers (PerkinElmer). X-Ray Powder Diffraction (XRD) was carried out on PANalytical X'Pert PRO MPD diffractometer with Cu Kα radiation (λ = 1.54178 Å). The isotherms were obtained using an ASAP 2020 Plus 2.0, and the specific surface area was calculated using the BET model. The samples were degassed at 80°C, under 5.10^{-3} mPa during 15 h. The adsorption was performed at 77K under nitrogen. X-ray photoelectron spectroscopy (XPS) measurement was conducted on Thermo Scientific K-Alpha.

Electrochemical measurements on the sulfur electrode. CVs and Galvanostatic discharge/charge (GCPL) measurements were performed in the voltage range of 1.60 to 3.0 V *vs.* Li^+/Li. EIS tests were performed on Bio-Logic® VMP3 multichannel potentiostat equipped with impedance modules in the frequency range of 0.1 MHz to 100 mHz. The composites FeCN-750@S_{60} and FeCN-950@S_{60} were mixed with 10 wt.% of Super P® (TIMCAL Super C65) as the conductive additive, and 10 wt.% of PVDF as the binder. Celgard®2335 was used as the separator and Li metal as the negative electrode, in a CR2032 coin cell system. The electrolyte consisted of 1.0 M LiTFSI, and 0.2 M of $LiNO_3$ in DOL and DME (1:1 in vol.). To increase the ratio of the active materials in the positive electrode, FeCN-950@S_{80} and FeCN-750@S_{80} including 64 wt.% of S in the final electrode and only 8 wt.% of carbon host material were also made (same proportions of Super P® and PVDF).

Results and discussion

Porous carbon xerogel including micro/mesopores with a high surface area was mixed with melamine as the nitrogen precursor and $Fe(ac)_2$ and treated at different temperatures (between 650°C to 1000°C) to dope carbon with nitrogen and introduce iron-based compounds (**Figure 1**). Melamine was chosen as the nitrogen precursor, due to the presence of six nitrogen atoms in its structure. The decomposition of melamine, after several steps, induces the formation of graphitic carbon nitride from 530°C[49]. In addition, it can release ammonia gas during the pyrolysis step. Ammonia gas at high temperature could increase the defect amounts into the carbon backbone and could promote the substitution of the carbon atoms with nitrogen (N-doped carbon)[26]. In addition, it could enhance the microporosity and thus the active surface area, which are key factors for sulfur impregnation and confinement of LiPSs in Li-S batteries.

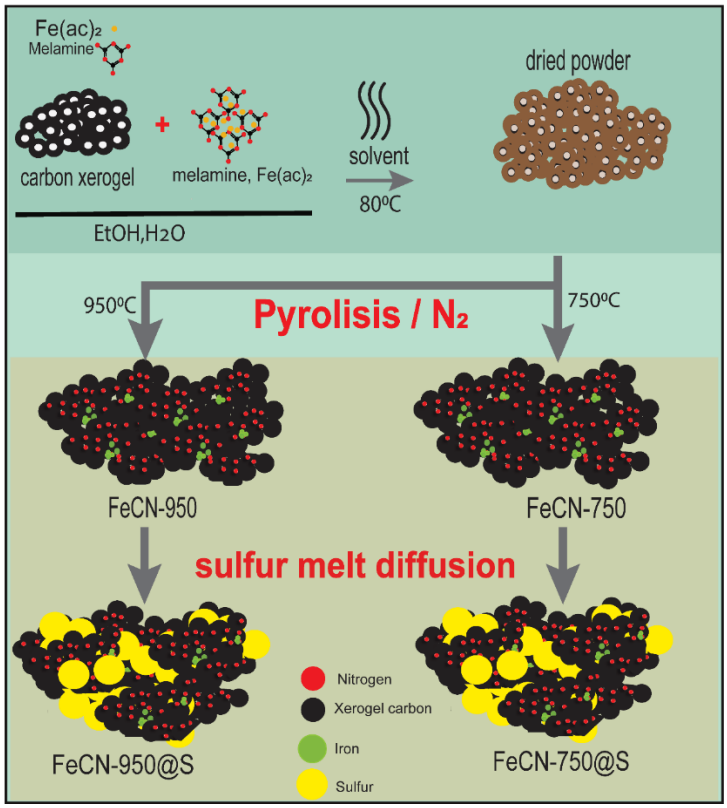

Figure 1: *Schematic representation of the step-by-step synthesis of FeCN-750@S and FeCN-950@S: The process involves the impregnation of porous carbon xerogel, characterized by micro- and mesopores, with Fe(II) atoms and melamine in a mixture of water and ethanol. This is followed by solvent evaporation and pyrolysis: at 750°C to produce FeCN-750 and at 950°C to yield FeCN-950. The final step involves sulfur impregnation by melt diffusion to form the composites FeCN-750@S and FeCN-950@S.*

The Secondary Electron Microscopy (SEM) images of the host carbon **(Figures 2 a-f)** is composed of large particles with a size between 5 and 10 µm, associated to the pyrolyzed carbon xerogel obtained after grinding, in accordance with the literature[50]. At high magnification, one can observe nanometric

nodules, about 10 nm in size. Independent of the thermal treatment, no visible modification in the carbon morphology can be observed with the addition of melamine, whatever the thermal treatment.

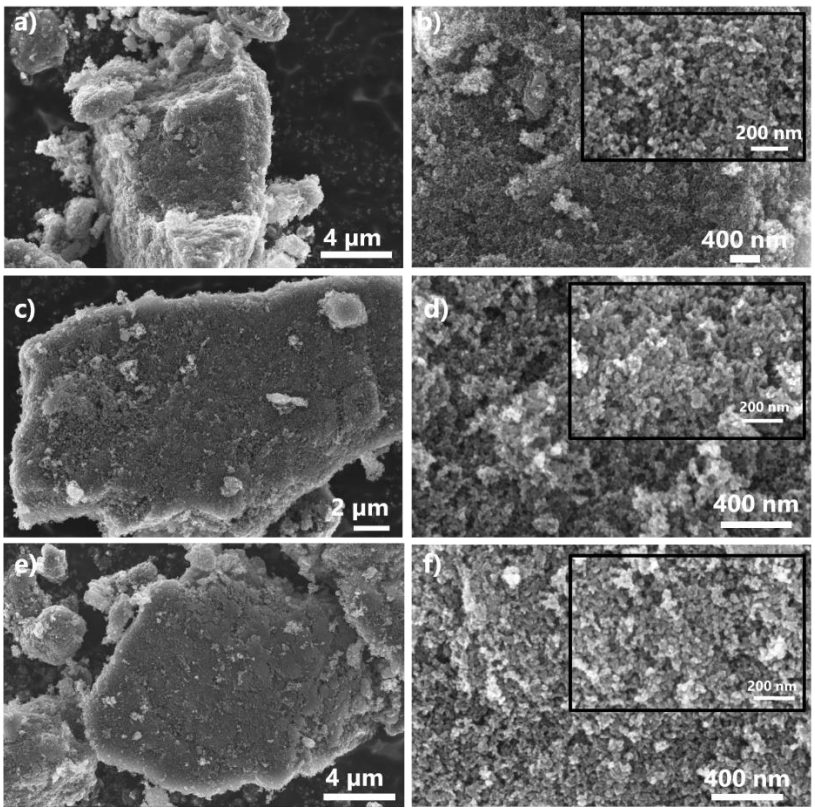

Figure 2. *Morphological characterizations of the sulfur host materials before doping and after doping in different temperature: SEM images captured at various magnifications, showcasing the morphology of the porous carbon xerogel and its nanostructure. The pristine carbon structure is illustrated in images* ***a,b)****, while the FeCN-750 and FeCN-950 samples are represented in images* ***c,d)*** *and* ***e,f)****, respectively.*

Transmission Electron Microscopy (TEM) was utilized to analyze the iron-based compounds, as shown in **Figures 3 a, b)** and **Figure S1**. It was observed that iron atoms aggregate into particles within the temperature range of 650°C to 800°C. Under these conditions, the porous carbon becomes adorned with iron-based particles, and their size decreases as the temperature increases. Notably, above 800°C, a carbon shell forms around the iron particles, as shown in the TEM images **(Figure S1)**, with the thickness of this shell increasing with increasing temperatures. The samples processed at 750°C and 950°C were selected for further investigations, representing two distinct iron morphologies: one without a carbon-based shell and the other with the carbon encapsulation of the iron particles.
Regardless of the pyrolysis temperature, the iron content in the final powders is approximately 0.5 wt.% as determined by atomic adsorption spectroscopy (AAS). The X-Ray diffraction (XRD) analysis was conducted to investigate the differences in iron phases between the two samples. The XRD patterns revealed three peaks at 2θ values of 25°, 45°, and 82°, which correspond to the characteristics of the porous carbon present in both samples **(Figure S2 a)**. Due to XRD's low sensitivity to small amounts of iron, the iron phases were undetectable at this concentration[51]. By increasing the iron content in the sample to a higher weight ratio of 2 wt.% and applying heat treatment at 950°C under nitrogen gas, peaks corresponding to Fe_3C were identified, indicating the formation of iron carbides at elevated iron concentrations **(Figure S2 b)**.

As the temperature increases, further changes in the carbon phase, specifically a transition toward more amorphous carbon, can be observed through Raman spectroscopy **(Figure 3 c, note S1)**[52]. For the FeCN-750 sample, the intensity of the D peak at 1340 cm^{-1} is lower than that of the G peak at 1608 cm^{-1}, yielding an intensity ratio of I_D/I_G = 0.77. In contrast, FeCN-950 exhibits a higher intensity for the D peak,

with an I_D/I_G ratio of 1.18. This suggests that increasing the temperature from 750°C to 950°C under nitrogen results in a greater number of defects within the carbon structure.
The surface area of the initial carbon xerogel is measured at 660 m^2g^{-1}. Following the addition of melamine, its decomposition at 750°C results in a slight decrease in specific surface area, reducing it to 600 m^2g^{-1}. In contrast, pyrolysis at 950°C leads to an increase in specific surface area, measuring 744 m^2g^{-1} **(Figure 3 d)**. This increase can be attributed to the gases released during melamine decomposition. Specifically, melamine and other nitrogen-containing solid compounds may initially reduce the surface area of the carbon host due to the precipitation of residual precursors within the porous structure. However, by employing a carefully controlled pyrolysis route (1 hour duration) and selecting an appropriate nitrogen precursor ratio (25 wt.%), it is possible to achieve samples with enhanced specific surface areas, consistent with findings in the literature[26].
The pristine xerogel, FeCN-750, and FeCN-950 samples exhibit Type I + IV isotherms, indicating microporous (with a high volume absorbed in the low relative pressure range) and mesoporous (with hysteresis at higher relative pressures) characteristics. This behavior aligns well with data in the literature and is supported by the mercury porosimetry technique results[47]. The specific surface area associated solely with microporosity, as determined by N_2 adsorption using the t-plot method, is 436 m^2g^{-1} for the pristine carbon. Following melamine addition and pyrolysis at 750°C, this value decreases to 375 m^2g^{-1} (14% reduction in surface area vs pristine carbon), likely due to melamine residues blocking the micropores. Increasing the pyrolysis temperature to 950°C enhances this value to 533 m^2g^{-1} (22% enhancement in surface area vs pristine carbon) due to the complete decomposition of melamine and the release of NH_3 gas. The type of porosity present in the carbon host materials can significantly influence Li-S battery performance, especially under lean electrolyte conditions, where the formation of LiPSs markedly increases electrolyte viscosity.

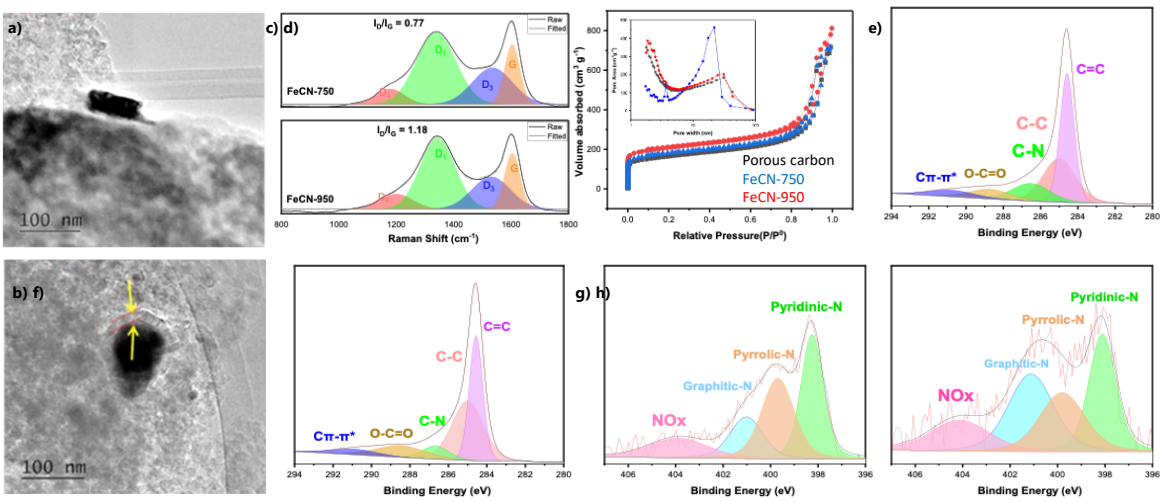

Figure 3. *The physiochemical characterization of the developed sulfur host materials: TEM images of the iron-based structures obtained with the same pyrolysis route with different final pyrolysis temperature,* ***a)*** *750 ℃ and* ***b)*** *950 ℃.* ***c)*** *Raman spectra of FeCN-750, and FeCN-950, including the calculated I_D/I_G.* ***d)*** *N_2 adsorption/desorption isotherm, and pore size distribution of the carbon xerogel, FeCN-750, and FeCN-950.* ***e, f)*** *C1s XPS spectra of sample FeCN-750 and FeCN-950, respectively.* ***g, h)*** *N1s XPS spectra of sample FeCN-750 and FeCN-950, respectively.*

The X-Ray Photoelectron Spectroscopy (XPS) measurements were conducted to further investigate the chemical composition of the FeCN-750 and FeCN-950 samples. The survey spectra clearly show that both FeCN-750 and FeCN-950 consist predominantly of carbon, with relatively low ratios of nitrogen and oxygen. Additionally, traces of iron are observed, attributable to the low wt.% of precursors used **(Figures S3 a and S3 b)** and in accordance with the 0.5 wt.% determine by AAS. The XPS survey spectra indicate that increasing the temperature to 950°C results in a reduction in the percentage of nitrogen

atoms at the surface compared to the sample obtained at 750°C, which could be partially associated to the formation of the carbon core shell at high pyrolyze temperature. In addition, EDX measurements were performed **(Figures S4 and S5)**, the mapping (**Figure S4)** confirms the uniform repartition of carbon, oxygen, nitrogen and Fe into the particles. The ratio of the main atoms obtained by EDX analysis highlights the lower amount of nitrogen for FeCN-950 than FeCN-750.

The C1s spectra for FeCN-750 and FeCN-950 can be deconvoluted into several components, exhibiting binding energies of 284.5 ± 0.2 eV, 285 ± 0.2 eV, 286.6 ± 0.2 eV, 288.5 ± 0.2 eV, and 291 ± 0.2 eV. These contributions are attributed to sp^2 and sp^3 carbon, C–N bonds, O=C–O groups, and π-π* satellite features, respectively **(Figures 3 e**, **f)**. Similarly, the N1s spectrum for FeCN-750 and FeCN-950 is deconvoluted into four distinct peaks, occurring at binding energies of 398.3 ± 0.2 eV, 399.6 ± 0.1 eV, 400.1 ± 0.2 eV, and 404 ± 0.2 eV, corresponding to pyridinic-N, pyrrolic-N, graphitic-N, and NOx species, respectively **(Figures 3 g, h)**[27–30]. The N1s spectrum indicates that the intensity of graphitic-N, in surface, is greater for FeCN-950, confirming that at this temperature (950°C), the N-doped carbon structures experience enhanced crystallization.

The polysulfide adsorption experiment **(Figure S6)** was performed by the UV-vis. The specific amount of the host materials (10 mg of FeCN-950 or FeCN-750) was added to 20 mL of 3 mM Li_2S_6 solution. A clear decrease in the intensity of the UV-vis peaks was observed, showing the absorption of LiPSs species with both FeCN-950 or FeCN-750. No significant difference is obtained for these two materials. Overall, the absorption property is insufficient to mitigate the PSs shuttle effect, indeed with a high sulfur/carbon-based host material ratio, the total trapping of LiPSs formed during cycling needs an uptake higher than a hundred percent of LiPSs per weight of host material, which is far for the absorption obtained.

Electrochemical characterization.

CV investigations

The kinetics of the polysulfide conversion reaction of Reaction 1 was studied by CV in three electrode system.

$$2S_6^{2-} + 2e^- \rightarrow 3S_4^{2-} \quad \textit{(reaction 1)}$$

CV was conducted at various scan rates, ranging from 10 mV s^{-1} to 100 mV s^{-1}, for the FeCN-950 and FeCN-750 samples **(Figures S7 a, b)**. The cathodic and anodic peaks are well-defined, and as expected, an increase in scan rate results in negative and positive shifts in the peak positions, respectively. The average k_0 values associated with reaction 1 were calculated to be approximately 1.6×10^{-4} cm s^{-1} for FeCN-950 and 7.2×10^{-5} cm s^{-1} for FeCN-750, determined using Nicholson's method. The higher k_0 value obtained for FeCN-950 indicates better catalytic activity of this host material for this specific reaction, which is attributed to the modification on the carbon support (presence of iron-based particles with or without a carbon core-shell structure). However, compared to the k_0 values observed for single iron atoms, this obtained values for FeCN-950 is lower by a factor of 2 to 4 [53]. The observed disparity in LiPSs conversion kinetics may be attributed to variations in the iron species' concentration and chemical state, and/or the morphology of the carbon support. Specifically, the single-atom iron catalyst (3 wt.% Fe) exhibits a different performance compared to the FeCN sample (0.5 wt.% Fe). This suggests that modifications to the carbon host structure significantly influence the rate-determining steps of LiPS conversion.

To further investigate the behavior of FeCN, the two host materials were impregnated with 60 wt.% sulfur, resulting in samples designated FeCN-950@S_{60} and FeCN-750@S_{60}. CV in two electrodes configuration was conducted at various scan rates, ranging from 0.1 mV s^{-1} to 0.5 mV s^{-1}, for electrodes prepared from FeCN-950@S_{60} and FeCN-750@S_{60}, within the voltage range of 1.60 V to 3.0 V *vs.* Li^+/Li **(Figures 4 a, b)**. The CVs of the FeCN-750@S_{60} and FeCN-950@S_{60} electrodes under mild conditions

(relatively low loading: 2 mg cm^{-2}; sufficient electrolyte quantity: E/S = 10 mL g^{-1}) display the characteristic lithiation/delithiation features typical of sulfur electrodes.

To analyze the reduction peaks, which are known to be sluggish reactions, Tafel curves were plotted from the CVs at scan rates of 0.1 to 0.5 mV s^{-1} **(Figures S8 a, b)**. For the reduction of S_8 to Li_2S_4 (first reduction peak), the fitted Tafel slopes for FeCN-950@S_{60} and FeCN-750@S_{60} were found to be 0.15 and 0.12 mV dec^{-1}, respectively. For the second reduction peak, corresponding to the nucleation of Li_2S, the Tafel slopes were 0.66 and 0.71 mV dec^{-1}, respectively. The higher slope values for this reaction are consistent with the lower kinetics associated with Li_2S formation. Both materials exhibit similar slopes at low sulfur loading and relatively high E/S ratios; however, the kinetics appears to be slightly lower for FeCN-950, which demonstrates greater polarization at higher scan rates.

Nyquist plots derived from EIS are shown in **Figure S9**. The Nyquist plot can be divided in three main regions. The high frequency (HF) region can be attributed to the ohmic contributions of the cell (electrolyte, electrical connections). The vertical straight line at low frequency (LF) is attributed to the blocking electronic charge transfer of sulfur electrode at OCV. The loop in the middle frequency (MF) region is associated with i) the existence of polarization through the composite electrode due to poor electronic contacts between sulfur and carbon particles[54] and ii) the passivation layer (Solid Electrolyte Interphase, SEI) on the lithium negative electrode. For cells based on FeCN-950@S_{60} and FeCN-750@S_{60}, only one main response is obtained, with near the same resistance. This identical response can be explained by the fact that it is associated with the SEI on the lithium surface[55]. No impedance response associated with the sulfur electrodes can be identified indicating good electronic percolation, consistent with the relatively low amount of sulfur.

Galvanostatic cycling test

(Figures 4 c, d) display the galvanostatic discharge/charge curves of the FeCN-750@S_{60}, FeCN-950@S_{60}, and C@S_{60} electrodes during the first cycle, all possessing a sulfur loading of 3.0 mg cm^{-2} with varying E/S ratios of 8 and 6 mL g^{-1}. For the E/S ratio of 8 mL g^{-1}, all electrodes demonstrate high discharge capacities of ~1200 mAh g^{-1}, representing 70% of the theoretical capacity at a rate of 0.1 C. The discharge curves feature a first plateau with a capacity of about 280 mAh g^{-1} (corresponding to 70% of sulfur into the electrode which was reduce into Li_2S_4), the capacity obtained during the second plateau, is consistent with a complete reduction of Li_2S_4 to Li_2S[56]. The cell capacity appears to be limited by sulfur accessibility, likely due to poor electrode wettability at low E/S ratio, rather than by Li_2S deposition, which is enhanced by the high surface area and the accessibility provided by the meso/macropores of the host carbon structures.

The discharge curve for FeCN-950@S_{60} exhibits greater polarization compared to both FeCN-750@S_{60} and C@S_{60}, consistent with the CV measurements. This overpotential may stem from the sluggish kinetics of LiPSs conversion reactions at low E/S ratios. Previous studies have demonstrated that low E/S ratios induce significant polarization during cycling, particularly during the Li_2S nucleation reaction stage[57]. Consequently, due to its higher void fraction, the FeCN-950 sample is likely more affected by low E/S ratios than both FeCN-750 and the pristine carbon structure. Additionally, the discharge curves for the FeCN-750@S_{60} and FeCN-950@S_{60} electrodes exhibit multiple discharge plateaus, contrasting with the two observed in C@S_{60}. This difference may be attributed to the confinement of various LiPS species within the micropores of the carbon structure (which are less than 2 nm in size) [28].

To investigate the effect of the E/S ratio on the performance of the electrodes, FeCN-950@S_{60}, FeCN-750@S_{60}, and C@S_{60} electrodes were assembled with an E/S ratio of 6 mL g^{-1}. Notably, all electrodes deliver high capacities even at this reduced E/S ratio **(Figure 4 d)**. However, the FeCN-950@S_{60} electrode displays the highest polarization during discharge at the onset of the second plateau, likely due to the

influence of micropores, consistent with the elevated polarization observed previously at the E/S ratio of 8 mL g^{-1}.

In contrast, the C@S_{60} sample exhibits a brief first plateau, significant polarization at the beginning of the second plateau, and poor reversibility, with only 850 mAh g^{-1} available on the first charge. The increased polarization observed in the samples with a lower E/S ratio may be attributed to the formation of a highly viscous catholyte, as the same amount of LiPSs is dissolved in a reduced volume of electrolyte. Additionally, the concentration of Li_2S_4 in this solution is relatively high (0.9 M equivalent; considering the amount of sulfur in the electrode and the volume of electrolyte used), yet the solubility of Li_2S_4 in a DOL/DME mixture has been reported to be limited to 0.1 M[58]. The poor reversibility noted for the C@S_{60} electrode may stem from the absence of nitrogen doping and the low polarity of the host carbon, both of which hinder the trapping of polysulfides.

Despite the slow kinetics of the electrochemical reaction, the moderate C-rate employed allows for a very high capacity in the first cycle, reaching 1400 mAh g^{-1} with the FeCN-950@S_{60} electrode. In this context, the high micropore volume, which contributes to a large surface area, facilitates the confinement of active species within the carbon structure, enabling the electrochemical reactions to occur and allowing for Li_2S deposition without passivating the 3D electrode.

The internal resistances of the cells with FeCN-750@S_{60} E/S=8 ml.g^{-1} and 6 ml.g^{-1} were determined during the galvanostatic test, at the end of charge and discharge, by measuring the ohmic drop of the cell. The changes in resistance values are shown in **Figure S10**. For the different E/S, the internal resistances of the cell are higher at the end of discharge than at the end of charge, which is due to the insulating nature of Li_2S, which passivates the carbon host material[55]. For both cells, a decrease in internal resistance is observed at the beginning of the cycling test, which may be associated with i) a decrease in the resistance of the SEI formed at the lithium/electrolyte interface, ii) a reorganization of the sulfur electrode with an improve of internal contact and/or iii) a decrease in the specific capacity of the cell inducing less sulfur or Li_2S deposited on the carbon surface. Regarding the impact of the amount of electrolyte, its decrease induces an increase in the internal resistance of the cell, which can be associated with an increase in the resistance of the electrolyte due to a higher concentration of soluble LiPSs, and with a decrease in the kinetics of the redox reaction due to the low solubility of highly concentrated LiPSs. The formation of Li_2S (end of discharge) is more affected than the formation of sulfur (end of charge).

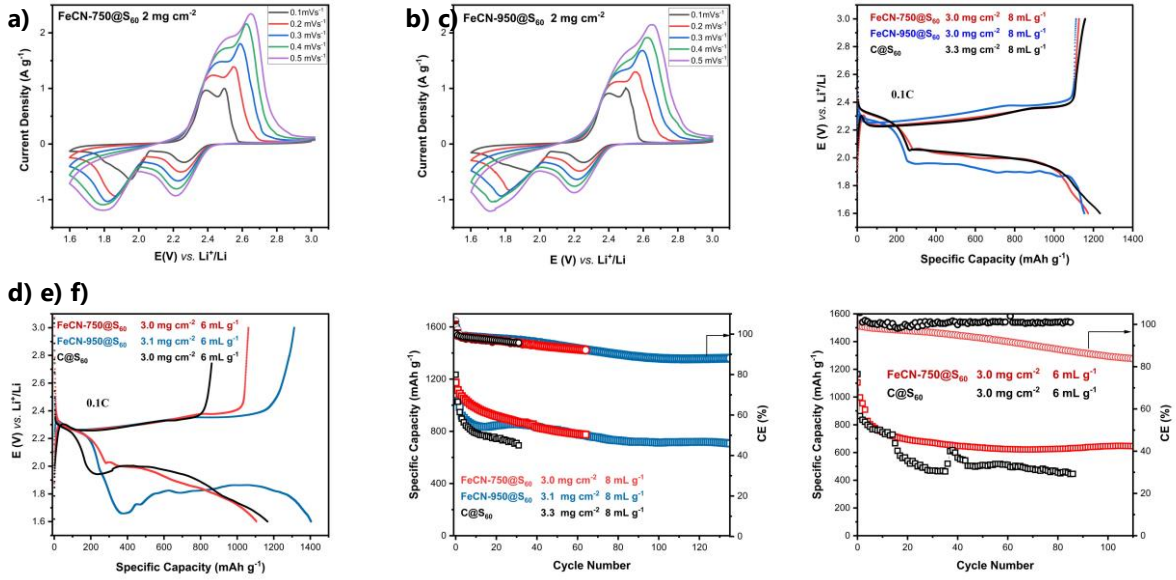

Figure 4. *Electrochemical performances of the cells using developed electrodes with 64%wt. sulfur in the sulfur host materials vs. lithium metal negative electrode: CV curves recorded at different scan rates (0.1 mV s^{-1} - 0.5 mV s^{-1}) for* ***a)*** *the cell using FeCN-750@S_{60} electrode, and* ***b)*** *FeCN-950@S_{60} electrode.* ***c)*** *and* ***d)*** *The first charge/discharge curves of the cells using FeCN-750@S_{60}, FeCN-950@S_{60} and C@S_{60} electrodes at 0.1C in different E/S ratios.* ***e)*** *Long-term stability of the cells using FeCN-750@S_{60}, FeCN-950@S_{60} and C@S_{60} electrodes at 0.1 C, E/S = 8 mL g^{-1}, and* ***f)*** *of cells using the FeCN-750@S_{60} and C@S_{60} electrodes at 0.1 C, E/S = 6 mL g^{-1}.*

Cyclability performance:

The cycling performance of the FeCN-950@S_{60}, FeCN-750@S_{60}, and C@S_{60} electrodes was assessed at a current density of 0.1 C **(Figure 4 e)**. The FeCN-950@S_{60} electrode demonstrates good cycling performance with an E/S ratio of 8 mL g^{-1}, achieving a discharge capacity of approximately 700 mAh g^{-1} and capacity retention above 64% after 140 cycles. In the case of the FeCN-750@S_{60}-based cell, after a gradual decline in the initial cycles, the discharge capacity stabilizes with a capacity retention of 63% after 64 cycles. Notably, there is no significant difference in capacity retention and coulombic efficiency (CE, n discharge/n charge) observed between these two host materials at E/S = 8 mL g^{-1}. On the other hand, the cell using C@S_{60} electrode shows a rapid capacity decay of 50% over 30 cycles. Given the comparable surface area and pore volume between FeCN-750 and the undoped porous carbon, the observed performance discrepancy is likely attributable to the increased polarity imparted by nitrogen doping and the presence of iron structures within the carbon matrix, both of which contribute to enhanced LiPSs retention or reaction kinetic. The CE starts near 100% but decreases during cycling, reaching around 88% for all electrodes. These CE values falling below 100% may arise from the well-known redox shuttle effect, which increases the charge process. The degradation of CE during cycling could also be associated with the deterioration of the lithium/electrolyte interphase, attributed to the consumption of $LiNO_3$ and the increase in lithium surface area during cycling, leading to unprotected lithium metal.[59]

Under lean electrolyte conditions (E/S = 6 mL g^{-1}), the Li-S cell employing FeCN-950@S_{60} electrode exhibited significant polarization, resulting in the suppression of the second discharge plateau and a substantial capacity fade **(Figure S11 b)**. In contrast, cells utilizing FeCN-750@S_{60} **(Figure S11 a)** and C@S60 **(Figure S11 c)** electrodes, despite possessing similar surface areas, demonstrated greater tolerance to the reduced E/S from 8 to 6 mL g^{-1}, retaining the characteristic two-plateau discharge profile. Specifically, the cell using FeCN-750@S_{60} electrode achieved superior capacity retention, maintaining 650 mAh g^{-1} over 100 cycles **(Figure 4 f)**, compared to the cell using C@S_{60} electrode **(Figure S12)**, which exhibited a capacity below 500 mAh g^{-1} under the same conditions, and a large polarization especially associated with the nucleation of the Li_2S at the beginning of the second

plateau[57]. The enhanced LiPSs confinement and capacity retention observed in FeCN-750, compared to the porous carbon control despite similar surface areas, suggests that the surface modifications introduced by the FeCN synthesis are crucial for improved electrochemical performance.

Sulfur content of 80 wt.%:

By increasing the sulfur content to ~84 wt.%, the electrochemical performance of the host materials was evaluated through CV and GCPL on the cell using the FeCN-950@S_{80} and FeCN-750@S_{80} electrodes. The CV obtained from the cell using FeCN-950@S_{80} electrode exhibits two cathodic peaks at 2.28 V and 1.95 V *vs.* Li^+/Li, as well as two anodic peaks at 2.40 V and 2.50 V *vs.* Li^+/Li, with a sulfur loading of 1.9 mg cm^{-2} and an E/S ratio of 15 mL g^{-1}. Similar peaks are observed for FeCN-750@S_{80} during the reduction process at 2.30 V and 2.0 V vs. Li^+/Li, and for the oxidation route at 2.35 V and 2.45 V vs. Li^+/Li **(Figure 5 a)**. This indicates lower polarization during both the reduction and oxidation processes, consistent with the observations made at a sulfur load of 60 wt.%.

The EIS spectra obtained at OCV from the cell using FeCN-950@S_{80} and FeCN-750@S_{80} show the same shape as those observed with 60 wt.% of sulfur with an increase of the impedance value obtained at MF. Furthermore, this response at MF appears to be composed of two semicircles, around 4000 Hz and 800-400 Hz (**Figure S13)**, the first semicircle (around 4000 Hz) may be related to the existence of polarization across the composite electrode due to poor electronic contacts associated with the higher amount of sulfur (80 wt.%) and its low electronic conductivity.

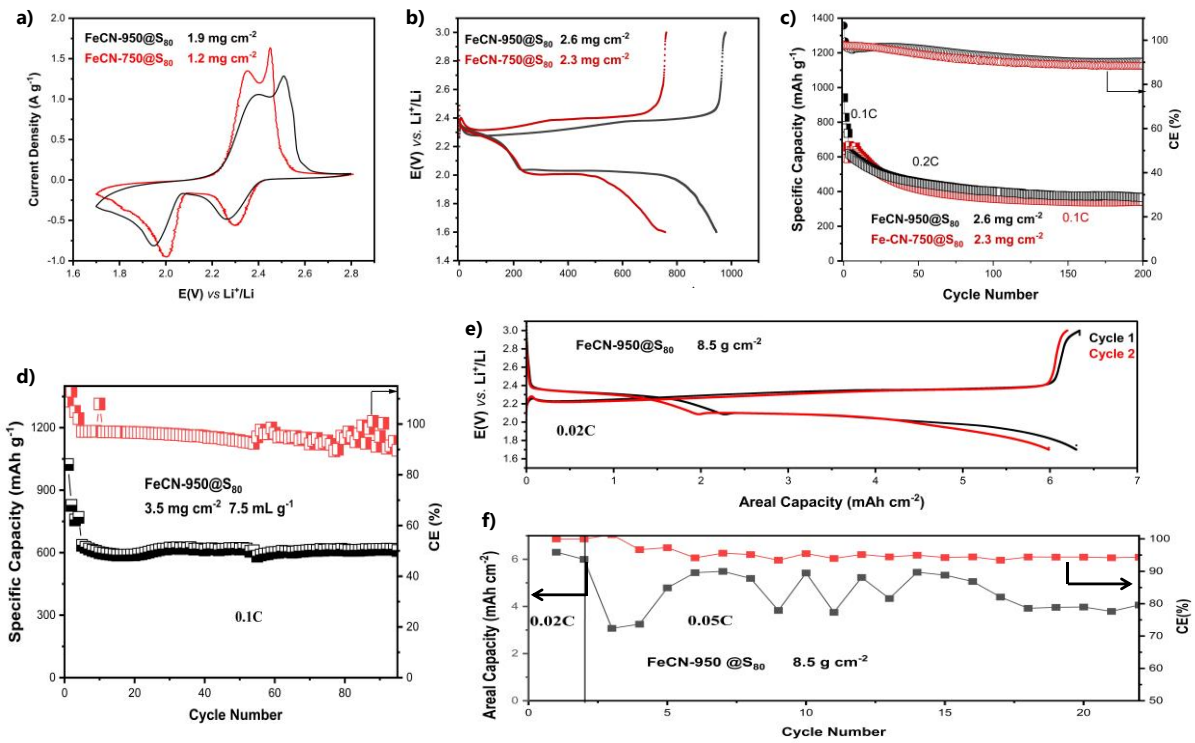

Figure 5. *Electrochemical performances of the cells using developed electrodes with 84%wt. sulfur in the sulfur host materials vs. lithium metal negative electrode:* ***a)*** *CV obtained from the cell using FeCN-750@S_{80} and FeCN-950@S_{80} electrodes at 0.1 mV s^{-1}.* ***b)*** *The GCPL curve of FeCN-750@S_{80} and FeCN-950@S_{80} electrodes at 0.1C.* ***c)*** *Long-term cycle stability of FeCN-750@S_{80} and FeCN-950@S_{80} electrodes at 0.1 C and 0.2 C, respectively.* ***d)*** *Long-term cycle stability of FeCN-950@S_{80} electrode, activation at 0.05 C and cycling at 0.1 C at lower E/S ratio (7.5 mL g^{-1}).* ***e)*** *GCPL curves (0.02C, first and second cycles), and* ***f)*** *cycling stability of cell using FeCN-950@S_{80} electrode with 8.5 mg cm^{-2} and 6.5 mL g^{-1}.*

The first charge/discharge curves for the cells using FeCN-750@S_{80} and FeCN-950@S_{80} electrodes at 0.1 C are compared in **Figure 5 b)**. For the cell with FeCN-750@S_{80} electrode discharge shows significant

polarization throughout the state-of-charge (SoC), with performance comparison opposite to that seen with 60 wt.% sulfur; here, FeCN-950@S_{80} exhibits superior performance. The main difference in the charge/discharge curves **(Figure 5 b)** is the length of the second plateau associated with Li_2S_2/Li_2S formation. The shorter second plateau for FeCN-750@S_{80} is likely due to its lower surface area (600 m^2 g^{-1} *vs.* 744 m^2 g^{-1}), limiting Li_2S_2/Li_2S precipitation onto the carbon surface[57].

The cycling stability results are shown in **Figure 5 c)**. After activation at 0.1 C, the FeCN-950@S_{80} electrode was cycled at 0.2 C for 240 cycles, achieving 67% capacity retention (390 mAh g^{-1}) by the fourth cycle. Conversely, cell with FeCN-750@S_{80} electrode, tested at 0.1 C, exhibited significant polarization, limiting its discharge capacity. During cycling, initially, its capacity increased from 590 to 660 mAh g^{-1} but then declined to 360 mAh g^{-1} after 100 cycles. The polarization of cell using FeCN-750@S_{80} electrode did not allow cycling at higher C-rate (i.e 0.2 C).

The internal resistances of the cells with FeCN-950@S_{60} E/S=8 ml.g^{-1} and FeCN-950@S_{80} 15 ml.g^{-1} were determined during the galvanostatic test, at the end of charge and discharge and are compared in **Figure S14**. As observed previously for FeCN-750@S_{60}-based cells, the resistance measured at the end of discharge is higher than that obtained at the end of charge for the FeCN-950@S_{60} E/S=8 ml.g^{-1} cell. For FeCN-950@S_{80} E/S=15 ml.g^{-1}, the internal resistances obtained at the end of charge and discharge are close and higher than those obtained with the other samples at the end of charge. This behavior may be linked to the low specific capacity obtained with such a high quantity of sulfur, in addition a high E/S allows good solubility of LiPSs and efficient reaction in the soluble state. The resistances of the FeCN-950@S_{80} cell, although higher, remain reasonable, explaining the good cycling results obtained.

To evaluate the electrochemical performance under lean electrolyte conditions (E/S = 7.5 mL g^{-1}), a cell using FeCN-950@S_{80} electrode with sulfur mass loading of 3.5 mg cm^{-2} was tested **(Figure 5 d)**. After activating at 0.02 C, discharge capacities of ~1000, 800, 760, and 750 mAh g^{-1} were observed in the first four cycles. Long-term stability tested at 0.1 C yielded a capacity of 600 mAh g^{-1} with ~96% retention over 95 cycles. Despite the low amount of electrolyte, the cell using FeCN-950@S_{80} electrode demonstrated high sulfur utilization and excellent cycling stability at high sulfur percentages. Its good performance might benefit from the enhancement in the polarity of the high surface area porous carbon after treatment.

For more challenging conditions, an electrode with 8.5 g cm^{-2} sulfur loading was tested at E/S = 6.5 mL g^{-1} at 0.02 C. It achieved a high areal capacity of 6.3 mAh cm^{-2} during the first two cycles, demonstrating no distortion in the voltage profile **(Figure 5 e)** and 100% coulombic efficiency. Under lean conditions, the combination of iron carbides and N-doped carbon with substantial micropore volume improves LiPS conversion kinetics and anchors soluble species to the electrode. The cycling stability of this electrode with ultra-high sulfur content (8.5 g cm^{-2}) was excellent, maintaining a capacity of 4 mAh cm^{-2} and a coulombic efficiency of ~94% over 22 cycles **(Figure 5 f)**, confirming great stability and reversibility. The comparison of this work with other literature highlights the exceptional electrochemical performance of the developed sulfur electrodes under challenging conditions **(Table S1)**.

Conclusion

We evaluated the effect of the E/S ratio on cell performance for carbon hosts with varying pore sizes and surface areas. For electrodes containing 60 wt.% sulfur, those using the FeCN-950 host demonstrated significant polarization at low E/S ratios (6 mL g^{-1}) due to their large pore fraction detrimental when the amount of electrolyte is low. In contrast, the FeCN-750 sample, with a lower pore fraction, achieved a discharge capacity of 650 mAh g^{-1} after 100 cycles at E/S = 6 mL g^{-1}. For electrodes with 80 wt.% sulfur, the FeCN-950 sulfur host attained a discharge capacity of 600 mAh g^{-1} with 96% capacity retention at 0.1 C over 100 cycles with an E/S ratio of 7.5 mL g^{-1}, in such high amount of sulfur, high surface area is the main property required to achieve high performance. These findings indicate that while enhancing the carbon host's polarity through nitrogen doping and the incorporation of Fe-

based particles improves LiPS adsorption and conversion kinetics, carbon hosts with high surface areas and physical confinement from micro- and mesoporosity are vital for retaining capacity at high sulfur content.

Acknowledgement

The authors thank Dr. Laetitia Dubau for performing the TEM analysis and Vincent Martin (LEPMI, Grenoble) for his assistance in performing XPS characterization. This research has benefited from the characterization equipment of the Grenoble INP – CMTC platform and the financial support of the Centre of Excellence of Multifunctional Architectured Materials ''CEMAM'' (grant ANR-10-LABX-44-01) funded by the ''Investments for the Future'' Program. We would like to thank the financial support from the ANR project. N° ANR-18-CE05-0022-01.

Supporting Information

Figure S1. TEM images of the iron-based structures
Figure S2. XRD patterns of FeCN-750 and FeCN-950 host carbon material
Figure S3. XPS survey of FeCN-750, and FeCN-950 sulfur hosts
Figures S4 and S5. EDX elemental mapping of the FeCN materials
Figure S6. UV-visible spectroscopy of FeCN-750 and FeCN-950 host carbon material
Figure S7. Cyclic voltammetry of FeCN-750, and FeCN-950 at different scan rates
Figure S8. Tafel curves of reduction peaks of FeCN-750@S_{60} and FeCN-950@S_{60} electrodes
Figure S9. Nyquist plot of FeCN-750@S_{60} and FeCN-950@S_{60} electrodes with 8 mL g^{-1} of electrolyte
Figure S10. Resistance evolutions of FeCN-750@S_{60} with E/S=8 ml.$g^{-1}$and E/S=6 ml.g^{-1}
Figure S11. GCPL curves of the FeCN-750@S_{60}, FeCN-950@S_{60}, C@S_{60} electrodes with E/S=6 mL g^{-1}
Figure S12. GCPL curves of the FeCN-750@S_{60}, FeCN-950@S_{60}, C@S_{60} electrodes with E/S=6 mL g^{-1}
Figure S13. Nyquist plot of FeCN-750@S_{80} and FeCN-950@S_{80} with 15 mL g^{-1} of electrolyte.
Figure S14. Resistance evolutions of FeCN-950@S_{60} and FeCN-950@S_{80}
Table S1. The comparison of this work with other literature data

References

(1) Pang, Q.; Liang, X.; Kwok, C. Y.; Nazar, L. F. Advances in lithium–sulfur batteries based on multifunctional cathodes and electrolytes. *Nature Energy* **2016**, *1* (9), 16132. DOI: 10.1038/nenergy.2016.132.
(2) Fang, X.; Peng, H. A Revolution in Electrodes: Recent Progress in Rechargeable Lithium–Sulfur Batteries. *Small* **2015**, *11* (13), 1488-1511. DOI: 10.1002/smll.201402354.
(3) Zhao, M.; Peng, H.-J.; Li, B.-Q.; Huang, J.-Q. Kinetic Promoters for Sulfur Cathodes in Lithium–Sulfur Batteries. *Accounts of Chemical Research* **2024**, *57* (4), 545-557. DOI: 10.1021/acs.accounts.3c00698.
(4) Guo, Y.; Niu, Q.; Pei, F.; Wang, Q.; Zhang, Y.; Du, L.; Zhang, Y.; Zhang, Y.; Zhang, Y.; Fan, L.; et al. Interface engineering toward stable lithium–sulfur batteries. *Energy & Environmental Science* **2024**, *17* (4), 1330-1367, DOI: 10.1039/D3EE04183B.
(5) Song, Y.-W.; Shen, L.; Yao, N.; Feng, S.; Cheng, Q.; Ma, J.; Chen, X.; Li, B.-Q.; Zhang, Q. Anion-Involved Solvation Structure of Lithium Polysulfides in Lithium–Sulfur Batteries. *Angewandte Chemie International Edition* **2024**, *63* (19), e202400343. DOI: 10.1002/anie.202400343.
(6) Huang, J.-Q.; Wang, Z.; Xu, Z.-L.; Chong, W. G.; Qin, X.; Wang, X.; Kim, J.-K. Three-dimensional porous graphene aerogel cathode with high sulfur loading and embedded TiO2 nanoparticles for advanced lithium–sulfur batteries. *Acs Applied Materials & Interfaces* **2016**, *8* (42), 28663-28670.

(7) Xie, K.; You, Y.; Yuan, K.; Lu, W.; Zhang, K.; Xu, F.; Ye, M.; Ke, S.; Shen, C.; Zeng, X.; et al. Ferroelectric-Enhanced Polysulfide Trapping for Lithium–Sulfur Battery Improvement. *Advanced Materials* **2017**, *29* (6), 1604724. DOI: 10.1002/adma.201604724.
(8) Chen, X.; Jiang, H.; Liu, J.-H.; Zhang, H.; Zhan, C.; Gao, Y.; Jiang, X.; Wang, Y.; Cao, X.; Chou, S.-L. Covalent Organic Frameworks and Their Derivatives for Applications in High-Performance Lithium–Sulfur Batteries. *Advanced Functional Materials* ***2025***,35(17), 2421697. DOI: 10.1002/adfm.202421697.
(9) Deng, D.-R.; Xiong, H.-J.; Luo, Y.-L.; Yu, K.-M.; Weng, J.-C.; Li, G.-F.; Lei, J.; Li, Y.; Zheng, M.-S.; Wu, Q.-H. Accelerating the Rate-Determining Steps of Sulfur Conversion Reaction for Lithium-Sulfur Batteries Working at an Ultrawide Temperature Range. *Advanced Materials* **2024**, *36* (39), 2406135. DOI: 10.1002/adma.202406135.
(10) Kong, W.; Yan, L.; Luo, Y.; Wang, D.; Jiang, K.; Li, Q.; Fan, S.; Wang, J. Ultrathin MnO2/Graphene Oxide/Carbon Nanotube Interlayer as Efficient Polysulfide-Trapping Shield for High-Performance Li–S Batteries. *Advanced Functional Materials* **2017**, *27* (18), 1606663. DOI: 10.1002/adfm.201606663.
(11) Zhai, S.; Ye, Z.; Liu, R.; Xu, H.; Li, C.; Liu, W.; Wang, X.; Mei, T. Defect Strategy-Regulated MoSe2-Modified Self-Supporting Graphene Aerogels Serving as Both Cathode and Interlayer of Lithium-Sulfur Batteries. *Advanced Functional Materials* **2024**, *34* (17), 2314379. DOI: 10.1002/adfm.202314379.
(12) Wang, L.; Liu, J.; Yuan, S.; Wang, Y.; Xia, Y. To mitigate self-discharge of lithium–sulfur batteries by optimizing ionic liquid electrolytes. *Energy & Environmental Science* **2016**, *9* (1), 224-231.
(13) Zhang, J.; Chou, J.; Luo, X.-X.; Yang, Y.-M.; Yan, M.-Y.; Jia, D.; Zhang, C.-H.; Wang, Y.-H.; Wang, W.-P.; Tan, S.-J.; et al. A Fully Amorphous, Dynamic Cross-Linked Polymer Electrolyte for Lithium-Sulfur Batteries Operating at Subzero-Temperatures. *Angewandte Chemie International Edition* **2024**, *63* (5), e202316087. DOI: 10.1002/anie.202316087.
(14) Lv, D.; Zheng, J.; Li, Q.; Xie, X.; Ferrara, S.; Nie, Z.; Mehdi, L. B.; Browning, N. D.; Zhang, J.-G.; Graff, G. L.; et al. High Energy Density Lithium–Sulfur Batteries: Challenges of Thick Sulfur Cathodes. *Advanced Energy Materials* **2015**, *5* (16), 1402290. DOI: 10.1002/aenm.201402290.
(15) Wu, F.; Ye, Y.; Chen, R.; Zhao, T.; Qian, J.; Zhang, X.; Li, L.; Huang, Q.; Bai, X.; Cui, Y. Gluing Carbon Black and Sulfur at Nanoscale: A Polydopamine-Based "Nano-Binder" for Double-Shelled Sulfur Cathodes. *Advanced Energy Materials* **2017**, *7* (3), 1601591.
(16) Lu, X.; Lian, G. J.; Parker, J.; Ge, R.; Sadan, M. K.; Smith, R. M.; Cumming, D. Effect of carbon blacks on electrical conduction and conductive binder domain of next-generation lithium-ion batteries. *Journal of Power Sources* **2024**, *592*, 233916. DOI: 10.1016/j.jpowsour.2023.233916.
(17) Chen, R.; Zhou, Y.; Li, X. Nanocarbon-enabled mitigation of sulfur expansion in lithium–sulfur batteries. *Energy Storage Materials* **2024**, *68*, 103353.
(18) Sun, L.; Wang, D.; Luo, Y.; Wang, K.; Kong, W.; Wu, Y.; Zhang, L.; Jiang, K.; Li, Q.; Zhang, Y. Sulfur embedded in a mesoporous carbon nanotube network as a binder-free electrode for high-performance lithium–sulfur batteries. *ACS nano* **2016**, *10* (1), 1300-1308.
(19) Yan, M.; Chen, H.; Yu, Y.; Zhao, H.; Li, C.-F.; Hu, Z.-Y.; Wu, P.; Chen, L.; Wang, H.; Peng, D.; et al. 3D Ferroconcrete-Like Aminated Carbon Nanotubes Network Anchoring Sulfur for Advanced Lithium–Sulfur Battery. *Advanced Energy Materials* **2018**, *8* (25), 1801066. DOI: 10.1002/aenm.201801066.
(20) Liu, B.; Wang, J.; Li, Z.; Sun, Z.; Li, C.; Seo, J.-M.; Li, J.; Guo, Y.; Yao, H.; Guan, S. Multiwall carbon nanotube-hyperbranched polymaleimide core–shell nanowires with hierarchical porous and polar structure as sulfur host for sustainable lithium-sulfur batteries. *Nano Energy* **2024**, *126*, 109611.
(21) Zhang, C.; Lv, W.; Zhang, W.; Zheng, X.; Wu, M.-B.; Wei, W.; Tao, Y.; Li, Z.; Yang, Q.-H. Reduction of Graphene Oxide by Hydrogen Sulfide: A Promising Strategy for Pollutant Control and as an Electrode for Li-S Batteries. *Advanced Energy Materials* **2014**, *4* (7), 1301565. DOI: 10.1002/aenm.201301565.
(22) Evers, S.; Nazar, L. F. Graphene-enveloped sulfur in a one pot reaction: a cathode with good coulombic efficiency and high practical sulfur content. *Chemical Communications* **2012**, *48* (9), 1233-1235.

(23) Lan, Y.; Wang, Y.; Wang, Y.; Lu, G.; Liu, L.; Tang, T.; Li, M.; Cheng, Y.; Xiao, J.; Li, X. Chip-inspired design of high-performance lithium–sulfur batteries by integrating monodisperse sulfur nanoreactors on graphene. *ACS nano* **2024**, *18* (24), 15638-15650.
(24) Li, Z.; Yin, L. Nitrogen-Doped MOF-Derived Micropores Carbon as Immobilizer for Small Sulfur Molecules as a Cathode for Lithium Sulfur Batteries with Excellent Electrochemical Performance. *ACS Applied Materials & Interfaces* **2015**, *7* (7), 4029-4038. DOI: 10.1021/am507660y.
(25) Yan, R.; Oschatz, M.; Wu, F. Towards stable lithium-sulfur battery cathodes by combining physical and chemical confinement of polysulfides in core-shell structured nitrogen-doped carbons. *Carbon* **2020**, *161*, 162-168. DOI: 10.1016/j.carbon.2020.01.046.
(26) Kensy, C.; Härtel, P.; Maschita, J.; Dörfler, S.; Schumm, B.; Abendroth, T.; Althues, H.; Lotsch, B. V.; Kaskel, S. Scalable production of nitrogen-doped carbons for multilayer lithium-sulfur battery cells. *Carbon* **2020**, *161*, 190-197. DOI: 10.1016/j.carbon.2020.01.037.
(27) Hong, X.-J.; Tang, X.-Y.; Wei, Q.; Song, C.-L.; Wang, S.-Y.; Dong, R.-F.; Cai, Y.-P.; Si, L.-P. Efficient Encapsulation of Small S2-4 Molecules in MOF-Derived Flowerlike Nitrogen-Doped Microporous Carbon Nanosheets for High-Performance Li–S Batteries. *ACS Applied Materials & Interfaces* **2018**, *10* (11), 9435-9443. DOI: 10.1021/acsami.7b19609.
(28) Han, P.; Chung, S.-H.; Manthiram, A. Pyrrolic-Type Nitrogen-Doped Hierarchical Macro/Mesoporous Carbon as a Bifunctional Host for High-Performance Thick Cathodes for Lithium-Sulfur Batteries. *Small* **2019**, *15* (16), 1900690. DOI: 10.1002/smll.201900690.
(29) Yan, Y.; Song, M.; Yang, Y.; Zhang, X.; Fan, C.; Xu, R.; Yang, Y.; Deng, Q.; Zhong, L.; Wang, X. Heteroatom doping carbon film derived from hyphae as a self-supporting cathode for advanced lithium sulfur batteries. *Applied Surface Science* **2024**, *659*, 159915.
(30) Wang, P.; Zeng, R.; You, L.; Tang, H.; Zhong, J.; Wang, S.; Yang, T.; Liu, J. Graphene-Like Matrix Composites with Fe2O3 and Co3O4 as Cathode Materials for Lithium–Sulfur Batteries. *ACS Applied Nano Materials* **2020**, *3* (2), 1382-1390. DOI: 10.1021/acsanm.9b02250.
(31) Wang, Z. Y.; Wang, L.; Liu, S.; Li, G. R.; Gao, X. P. Conductive CoOOH as carbon-free sulfur immobilizer to fabricate sulfur-based composite for lithium–sulfur battery. *Advanced Functional Materials* **2019**, *29* (23), 1901051.
(32) He, J.; Chen, Y.; Manthiram, A. Metal sulfide-decorated carbon sponge as a highly efficient electrocatalyst and absorbant for polysulfide in high-loading Li2S batteries. *Advanced Energy Materials* **2019**, *9* (20), 1900584.
(33) Zhu, G.; Wu, Q.; Zhang, X.; Bao, Y.; Zhang, X.; Shi, Z.; Zhang, Y.; Ma, L. Designing metal sulfide-based cathodes and separators for suppressing polysulfide shuttling in lithium-sulfur batteries. *Nano Research* **2024**, *17* (4), 2574-2591.
(34) Nguyen, V. P.; Kim, I. H.; Shim, H. C.; Park, J. S.; Yuk, J. M.; Kim, J.-H.; Kim, D.; Lee, S.-M. Porous carbon textile decorated with VC/V2O3-X hybrid nanoparticles: Dual-functional host for flexible Li-S full batteries. *Energy Storage Materials* **2022**, *46*, 542-552. DOI: 10.1016/j.ensm.2022.01.027.
(35) Wang, J.; Han, W.-Q. A Review of Heteroatom Doped Materials for Advanced Lithium–Sulfur Batteries. *Advanced Functional Materials* **2022**, *32* (2), 2107166. DOI: 10.1002/adfm.202107166.
(36) He, Q.; Chen, W.; Fan, B.; Wei, Q.; Zou, Y. Heteroatom-doped ZIF-67 for anchoring and catalyzing polysulfides in lithium–sulfur batteries. *Chemical Engineering Journal* **2024**, *496*, 153813.
(37) Wang, Y.; Li, M.; Xu, L.; Tang, T.; Ali, Z.; Huang, X.; Hou, Y.; Zhang, S. Polar and conductive iron carbide@ N-doped porous carbon nanosheets as a sulfur host for high performance lithium sulfur batteries. *Chemical Engineering Journal* **2019**, *358*, 962-968.
(38) Tiwari, S.; Yadav, V.; Poonia, A.; Pal, D. Exploring advances in sulfur composite cathodes for lithium-sulfur batteries: A comprehensive review. *Journal of Energy Storage* **2024**, *94*, 112347.
(39) Cao, G.; Li, X.; Chen, L.; Duan, R.; Li, J.; Jiang, Q.; Wang, J.; Li, M.; Li, M.; Wang, J. Tuning Redox Behavior of Sulfur Cathodes Via Ternary-Coordinated Single Fe Atom in Lithium-Sulfur Batteries. *Small* **2024**, *20* (24), 2311174.
(40) Wang, Q.; Kim, H.; Li, Z.; Song, L.; Yoon, W.-S.; Bulakhe, R. N.; Kim, J. M. Propelling polysulfides conversion in lithium-sulfur batteries via separator modification with nitrogen-doped porous carbon nanosheets decorated by iron carbide nanoparticles. *Chemical Engineering Journal* **2025**, 160588.

(41) Zhu, Q.-C.; Ye, C.; Xiang, T.; Yang, X.-B.; Mao, D.-Y. Improved performance of lithium–sulfur battery with a free-standing cobalt-doped vanadium nitride carbon nanofiber interlayer. *Journal of Electroanalytical Chemistry* **2024**, *958*, 118164. DOI: 10.1016/j.jelechem.2024.118164.
(42) Liu, J.; Yu, L.; Ran, Q.; Chen, X. a.; Wang, X.; He, X.; Jin, H.; Chen, T.; Chen, J. S.; Guo, D. Regulating Electron Filling and Orbital Occupancy of Anti-Bonding States of Transition Metal Nitride Heterojunction for High Areal Capacity Lithium–Sulfur Full Batteries. *Small* **2024**, *20* (31), 2311750.
(43) Si, J.; Zhao, M.; Cui, Z.; Cai, D.; Zhan, H.; Wang, Q. Crystalline and amorphous Fe2O3 nanocubes grown on electrospun carbon nanofibers for lithium-ion batteries and lithium-sulfur batteries: A comparative study. *Applied Surface Science* **2024**, *657*, 159782.
(44) Zhao, Z.; Dou, H.; Xu, X.; Zhe, R.; Zhao, Q.; Zheng, L.; Bao, X.; Zhu, T.; Wang, H.-E. Magnetopyrite Fe1− xS modified with N/S-doped carbon as a synergistic electrocatalyst for lithium-sulfur batteries. *Journal of Colloid and Interface Science* **2025**, *684*, 180-191.
(45) Liu, Y.-T.; Liu, S.; Li, G.-R.; Yan, T.-Y.; Gao, X.-P. High Volumetric Energy Density Sulfur Cathode with Heavy and Catalytic Metal Oxide Host for Lithium–Sulfur Battery. *Advanced Science* **2020**, *7* (12), 1903693. DOI: 10.1002/advs.201903693.
(46) Yuan, Z.; Peng, H. J.; Hou, T. Z.; Huang, J. Q.; Chen, C. M.; Wang, D. W.; Cheng, X. B.; Wei, F.; Zhang, Q. Powering Lithium-Sulfur Battery Performance by Propelling Polysulfide Redox at Sulfiphilic Hosts. *Nano Lett* **2016**, *16* (1), 519-527. DOI: 10.1021/acs.nanolett.5b04166.
(47) Rey-Raap, N.; Piedboeuf, M.-L. C.; Arenillas, A.; Menéndez, J. A.; Léonard, A. F.; Job, N. Aqueous and organic inks of carbon xerogels as models for studying the role of porosity in lithium-ion battery electrodes. *Materials & Design* **2016**, *109*, 282-288.
(48) Nicholson, R. S. Theory and Application of Cyclic Voltammetry for Measurement of Electrode Reaction Kinetics. *Analytical Chemistry* **1965**, *37* (11), 1351-1355. DOI: 10.1021/ac60230a016.
(49) Lotsch, B. V.; Schnick, W. New light on an old story: formation of melam during thermal condensation of melamine. *Chemistry* **2007**, *13* (17), 4956-4968. DOI: 10.1002/chem.200601291.
(50) Piedboeuf, M.-L. C.; Léonard, A. F.; Deschamps, F. L.; Job, N. Carbon xerogels as model materials: toward a relationship between pore texture and electrochemical behavior as anodes for lithium-ion batteries. *Journal of Materials Science* **2016**, *51* (9), 4358-4370. DOI: 10.1007/s10853-016-9748-3.
(51) Huan, T. N.; Ranjbar, N.; Rousse, G.; Sougrati, M.; Zitolo, A.; Mougel, V.; Jaouen, F.; Fontecave, M. Electrochemical reduction of CO2 catalyzed by Fe-NC materials: A structure–selectivity study. *ACS catalysis* **2017**, *7* (3), 1520-1525.
(52) Cuesta, A.; Dhamelincourt, P.; Laureyns, J.; Martínez-Alonso, A.; Tascón, J. M. D. Raman microprobe studies on carbon materials. *Carbon* **1994**, *32* (8), 1523-1532. DOI: 10.1016/0008-6223(94)90148-1.
(53) Rahimi, S.; Stievano, L.; Dubau, L.; Iojoiu, C.; Lecarme, L.; Alloin, F. Single-Atomic Dispersion of Fe and Co Supported on Reduced Graphene Oxide for High-Performance Lithium–Sulfur Batteries. *ACS Applied Materials & Interfaces* **2023**, 15(38), 44932−44941. DOI: 10.1021/acsami.3c08669.
(54) Seid K.A.; Badot J.C.; Dubrunfaut, O; Levasseur, S.; Guyomard, D.; Lestriez, B. Multiscale electronic transport mechanism and true conductivities in amorphous carbon–LiFePO4 nanocomposites, J. Mater. Chem. 22 (2012) 2641–2649.DOI: 10.1039/C2JM13429B.
(55) Walus, S.; Alloin F.; Barchasz, C.; Bouchet R. Electrochemical impedance spectroscopy study of Lithium–Sulfur batteries: Useful technic to go deeper in the Li/S electrochemical mechanism Electrochimica Acta, 359, 136944, 2020.DOI: https://doi.org/10.1016/j.electacta.2020.136944.
(56) Waluś, S.; Barchasz, C.; Bouchet, R.; Leprêtre, J.-C.; Colin, J.-F.; Martin, J.-F.; Elkaïm, E.; Baehtz, C.; Alloin, F. Lithium/Sulfur Batteries Upon Cycling: Structural Modifications and Species Quantification by In Situ and Operando X-Ray Diffraction Spectroscopy. *Advanced Energy Materials* **2015**, *5* (16), 1500165. DOI: 10.1002/aenm.201500165.
(57) Chen, Z.-X.; Cheng, Q.; Li, X.-Y.; Li, Z.; Song, Y.-W.; Sun, F.; Zhao, M.; Zhang, X.-Q.; Li, B.-Q.; Huang, J.-Q. Cathode Kinetics Evaluation in Lean-Electrolyte Lithium–Sulfur Batteries. *Journal of the American Chemical Society* **2023**, *145* (30), 16449-16457. DOI: 10.1021/jacs.3c02786.

(58) Pan, H.; Wei, X.; Henderson, W. A.; Shao, Y.; Chen, J.; Bhattacharya, P.; Xiao, J.; Liu, J. On the way toward understanding solution chemistry of lithium polysulfides for high energy Li–S redox flow batteries. *Advanced Energy Materials* **2015**, *5* (16), 1500113.
(59) Zhang, S. S. Role of LiNO3 in rechargeable lithium/sulfur battery. *Electrochimica Acta* **2012**, *70*, 344-348.